

Gain-scheduled \mathcal{H}_∞ buckling control of a circular beam-column subject to time-varying axial loads

Maximilian Schaeffner ¹ and Roland Platz ²

¹ Technische Universität Darmstadt, System Reliability, Adaptronics and Machine Acoustics SAM, Magdalenenstraße 4, 64289 Darmstadt, Germany, schaeffner@sam.tu-darmstadt.de

² Fraunhofer Institute for Structural Durability and System Reliability LBF, Bartningstraße 47, 64289 Darmstadt, Germany

ABSTRACT

For slender beam-columns loaded by axial compressive forces, active buckling control provides a possibility to increase the maximum bearable axial load above that of a purely passive structure. In this paper, an approach for gain-scheduled \mathcal{H}_∞ buckling control of a slender beam-column with circular cross-section subject to time-varying axial loads is investigated experimentally. Piezo-elastic supports with integrated piezoelectric stack actuators at the beam-column ends allow an active stabilization in arbitrary lateral directions. The axial loads on the beam-column influence its lateral dynamic behavior and, eventually, cause the beam-column to buckle. A reduced modal model of the beam-column subject to axial loads including the dynamics of the electrical components is set up and calibrated with experimental data. Particularly, the Linear Parameter-Varying (LPV) open-loop plant is used to design a model-based gain-scheduled \mathcal{H}_∞ buckling control that is implemented in an experimental test setup. The beam-column is loaded by ramp- and step-shaped time-varying axial compressive loads that result in a lateral deformation of the beam-column due to imperfections, such as predeformation, eccentric loading or clamping moments. The lateral deformations and the maximum bearable loads of the beam-column are analyzed and compared for the beam-column with and without gain-scheduled \mathcal{H}_∞ buckling control or, respectively, active and passive configuration. With the proposed gain-scheduled \mathcal{H}_∞ buckling control it is possible to increase the maximum bearable load of the active beam-column by 19% for ramp-shaped axial loads and to significantly reduce the beam-column deformations for step-shaped axial loads compared to the passive structure.

Keywords: gain-scheduled \mathcal{H}_∞ control, Linear Parameter-Varying (LPV) system, time-varying axial load, buckling control

1 INTRODUCTION

Slender beam-columns are common elements of mechanical load-carrying structures such as lightweight truss structures that are subject to time-varying axial and lateral loads or bending moments. Buckling of the slender beam-columns due to axial compressive loads represents a critical design constraint for these structures. For passive beam-columns subject to (quasi-)static axial loads, the theory of buckling has been thoroughly investigated for both ideal and imperfect structures, [1]. Vibration and buckling of passive beam-columns subject to time-varying axial loads has also been investigated so far, [2, 3]. In general, imperfect beam-columns exhibit large lateral deformations for axial loads considerably below the theoretical critical buckling load and, therefore, have lower maximum bearable axial loads. A common approach to passively increase the maximum bearable axial load is to change the geometry, e. g. length and cross-section area, or the material so that the beam-column withstands higher loads. This, however, is sometimes not desirable because of given design constraints. In these cases, active buckling control without significant change in the beam-column's geometry and material properties provides a suitable approach to increase the maximum bearable axial load of a given structure.



License: CC BY-NC-ND 4.0 International - Creative Commons, Attribution, Non Commercial, No Derivatives

Active buckling control of slender beam-columns with different boundary conditions has been investigated numerically and experimentally in the past several times, [4–10]. All of these investigated structures, though, have rectangular cross-sections, relatively high slenderness ratios λ , with $300 \leq \lambda \leq 1760$, and relatively low absolute values of the theoretical critical buckling load $F_{x,\text{cr}}$, with $5 \text{ N} \leq F_{x,\text{cr}} \leq 151 \text{ N}$. Both, slenderness ratios and critical buckling loads, are not realistic for typical applications. Furthermore, the structures are subject to (quasi-) static axial loads and controllers are also static or switched manually. Also, often surface bonded piezoelectric patches are applied to beam-columns with rectangular cross-section to induce active bending moments that counteract the deformation, [4–8]. However, the piezoelectric patches are exposed to the surroundings and also significantly modify the original beam-column stiffness. The active stabilization concept investigated by earlier own studies uses piezoelectric stack actuators to apply active lateral forces near the base of a fixed-pinned beam-column with rectangular cross-section, [9–11]. This way, the surface is kept free of applied piezoelectric patch actuators.

To the authors' knowledge, active buckling control of beam-columns with circular cross-section has not yet been investigated except in own works, [12–14]. In [12, 13], active buckling control of a circular beam-column with relatively low slenderness ratio $\lambda = 108$ and relatively high critical buckling load $F_{x,\text{cr}} = 3194 \text{ N}$, which seem to be more realistic for real structures, is investigated numerically and experimentally. The beam-column is supported by piezo-elastic supports in which active lateral forces of piezoelectric stack actuators are transformed into bending moments acting in arbitrary directions at the beam-column's ends. With this concept, no active manipulation is needed at the beam-column's surface. The beam-column is stabilized by an integral linear quadratic control (LQR) for (quasi-)static axial loads. The integral LQR is able to compensate initial deformation that may lead to buckling and is able to increase the maximum bearable load of the beam-column in numerical simulation and experiment. In [14], a Linear Parameter-Varying (LPV) control approach is successfully implemented for the same slender beam-column with an enhanced version of piezo-elastic supports resulting in slenderness ratio $\lambda = 95$ and critical buckling load $F_{x,\text{cr}} = 3864 \text{ N}$. Other investigations on active buckling control of beam-columns subject to time-varying axial loads with controllers that account for the axial load-dependency of the lateral beam-column dynamics are not known to the authors.

Now, in this paper, a gain-scheduled \mathcal{H}_∞ buckling control of the beam-column system from [14] is investigated experimentally. The beam-column is loaded by ramp- and step-shaped time-varying axial compressive loads resulting in a lateral deformation of the passive beam-column due to imperfections. The active beam-column is stabilized and is able to bear higher axial loads. This paper is organized as follows: First, the investigated beam-column system with piezo-elastic supports and the experimental test setup are presented. Then, the mathematical model of the beam-column system based on a FE model, which is reduced by modal truncation and extended by electrical components, is presented. Next, the mathematical model, which is extended by frequency-dependent weights to tune the controller, is used for synthesis of the model-based gain-scheduled \mathcal{H}_∞ buckling control. Finally, experimental results of the active buckling control for ramp- and step-shaped axial loads are presented and compared to the passive beam-column without gain-scheduled \mathcal{H}_∞ buckling control.

2 SYSTEM DESCRIPTION

In the following, the investigated beam-column with piezo-elastic supports and the experimental test setup for active buckling control are presented. The investigated structure is a slender beam-column made of aluminum alloy EN AW-7075 with length $l_b = 400 \text{ mm}$ and circular solid cross-section with radius $r_b = 4 \text{ mm}$, figure 1. The Young's modulus $E_b = 71.0 \cdot 10^3 \text{ N/mm}^2$ and density $\rho_b = 2.85 \cdot 10^{-3} \text{ g/mm}^3$ are assumed to be constant across the entire beam-column length. The beam-column is embedded in two piezo-elastic supports A at location $x = 0 \text{ mm}$ and B at $x = l_b$. The lower support A is fixed in axial and lateral directions. The upper support B is also fixed laterally, but is free to move in axial direction so that a time-varying axial load $F_x(t)$ may be applied, figure 1a. Strain gauges at the sensor position $x_s = l_b/2 = 200 \text{ mm}$ are used to measure the surface strains of the beam-column in y - and z -direction. Imperfections such as predeformation, eccentric loading or clamping moments in the real beam-column system are represented by disturbance bending moments $M_{d,y/z}(t)$ acting in opposite directions at supports A and B in the mathematical model, see section 3.1.

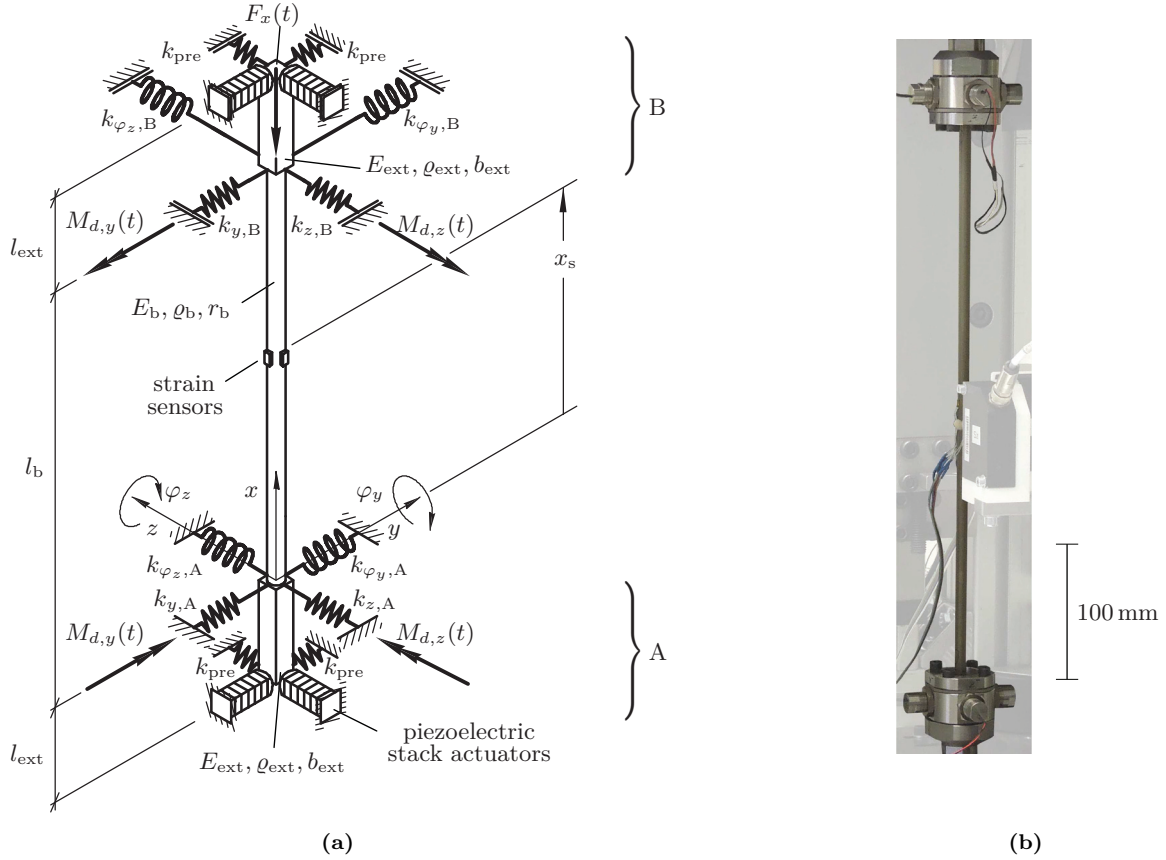


Fig. 1 Beam-column system, (a) schematic sketch of beam-column, (b) beam-column with piezo-elastic supports for experiments

Figure 2 shows sectional views of the piezo-elastic support A. The central element of the support are two concave-shaped elastic membrane springs made of spring steel 1.1248. They are manufactured by an incremental sheet metal forming process, [15], and bear the axial and lateral loads and allow rotations in any plane perpendicular to the x -axis, figures ?? and ?. In the schematic sketch, figure 1a, the elastic support properties from the elastic membrane springs clamped in the support housings are represented by rotational stiffness $k_{\varphi_y,A} = k_{\varphi_z,A} = k_{\varphi_y,B} = k_{\varphi_z,B} = k_r$ and lateral stiffness $k_{y,A} = k_{z,A} = k_{y,B} = k_{z,B} = k_l$ that are the same for both supports A and B and in y - and z -direction, section 3.1.3. In each piezo-elastic support A and B at $x = -l_{ext}$ and $x = l_b + l_{ext}$ in figure 1a, two piezoelectric stack actuators PI Ceramic® *P-887* are arranged orthogonal to each other and orthogonal to the beam-column's x -axis, acting in y - and z -direction, figure 2. Each actuator is mechanically prestressed by an allocated preload spring with stiffness $k_{pre} = 170 \text{ N/mm}$ that is relatively small and, thus, is neglected in the following. The piezoelectric stack actuators exert lateral forces to the beam-column's axial extensions with quadratic cross-section and relatively high bending stiffness made of hardened steel 1.4301 with length $l_{ext} = 8.9 \text{ mm}$, edge length $b_{ext} = 6 \text{ mm}$, Young's modulus $E_{ext} = 210.0 \cdot 10^3 \text{ N/mm}^2$ and density $\varrho_{ext} = 7.81 \cdot 10^{-3} \text{ g/mm}^3$. The extension works as a cantilever beam end beyond the elastic membrane springs for each support A and B. This way, the active lateral forces provided by the piezoelectric stack actuators act in arbitrary directions orthogonal to the beam-column's longitudinal x -axis. They result in bending moments that act in arbitrary directions at the beam-column ends in both piezo-elastic supports A and B.

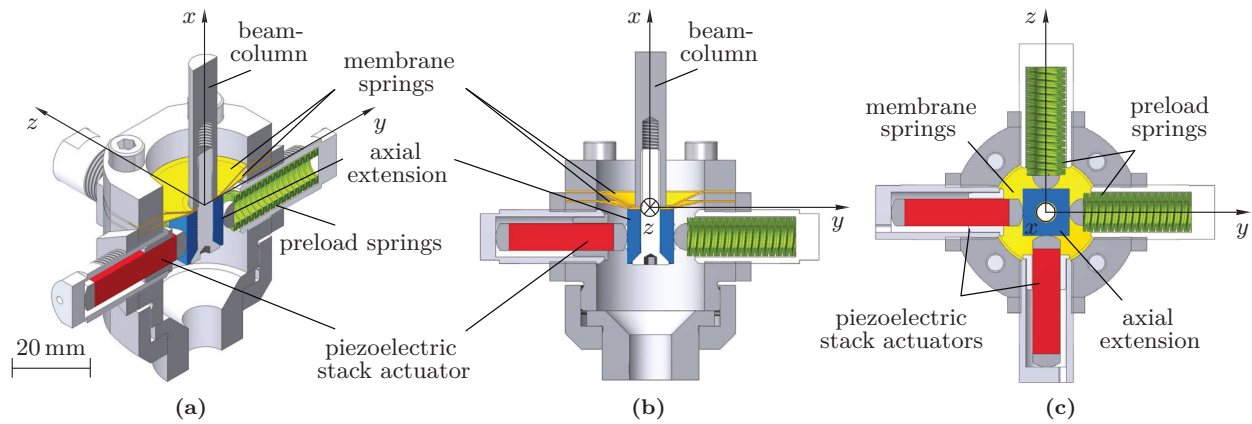


Fig. 2 Sectional views of piezo-elastic support A, (a) 3D section through x - y -plane, (b) 2D section through x - y -plane, (c) 2D section bottom view through actuator-plane

The data acquisition and the controller implementation are performed with a dSPACE® *DS1103* real-time platform with a sampling rate of 5000 Hz. All sensor signals are amplified and filtered prior to A/D conversion by a PEEKEL® *PICAS* strain gauge amplifier. The real-time platform output voltages are filtered by KEMO® *BenchMaster 21M* reconstruction filters and amplified by Piezomechanik® *LE 150/200* piezo amplifiers before being applied to the piezoelectric stack actuators in piezo-elastic supports A and B.

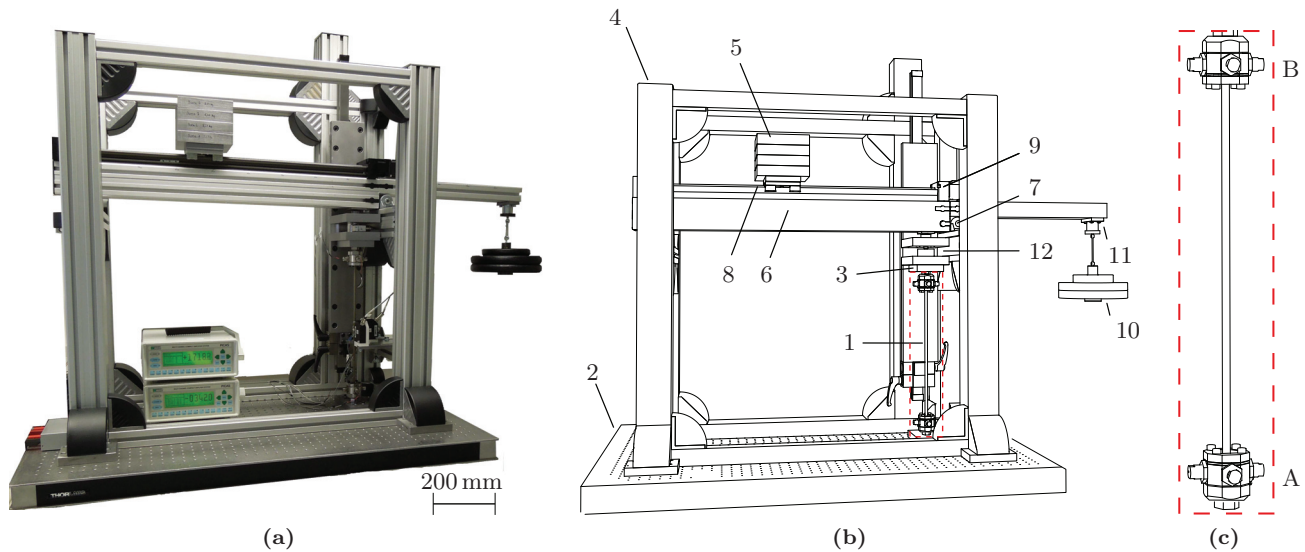


Fig. 3 Experimental test setup for active buckling control, (a) photo of test setup, (b) CAD sketch of test setup (without strain gauge amplifiers), (c) CAD sketch of beam-column with piezo-elastic supports 1

Figure 3 shows a photo and CAD sketches of the experimental test setup for the axially loaded beam-column with piezo-elastic supports 1 from figure 1b. The lower piezo-elastic support A is fixed on a baseplate 2 and the upper piezo-elastic support B is fixed to a parallel guidance 3 that is connected to a stiff frame structure 4. The beam-column is loaded via a high lever ratio by a mass 5 up to 30 kg that is placed on a stiff beam 6, which is supported by a hinge 7. The lever ratio and, therefore, the axial load are increased by shifting the mass in nearly horizontal plane via a linear axle 8, operated by a stepper motor 9. An additional optional weight 10 of up to 15 kg reduces the axial load on the beam-column. It can be released by an electromagnet 11, thus generating an approximately step-shaped axial compressive load. The axial load is measured by a load cell 12. With the presented test setup, ramp-shaped axial loads between the static load $F_{x,\min} = 337$ N of the parallel guidance 3, and $F_{x,\max} \approx 5000$ N as well as step-shaped axial loads of up to $F_{\text{step}} = 1000$ N are realizable.

3 MATHEMATICAL MODEL OF BEAM-COLUMN SYSTEM

In the following section, the mathematical model used for the design of a model-based gain-scheduled \mathcal{H}_∞ buckling control of the axially loaded beam-column is derived. The performance of model-based controllers is primarily determined by the quality of the underlying mathematical model. In particular, the model has to properly describe the complex boundary conditions created by the piezo-elastic supports and has to include the actuators and sensors in the system. Furthermore, the axial load-dependency of the beam-column that is prone to buckle has to be considered as a Linear Parameter-Varying (LPV) system.

In this chapter, first a finite element (FE) model that meets all named requirements is presented. Second, the FE model is reduced by modal truncation to reduce the order and complexity for controller synthesis. Third, the dynamics of the electrical components for signal conditioning, such as analog filters and amplifiers, are added to the lateral beam-column dynamics to account for the existing phase delay. Finally, numerical simulations of the overall beam-column system dynamics are compared to experimental results.

3.1 FE MODEL OF BEAM-COLUMN SYSTEM

The lateral vibration of the axially loaded beam-column is described by a FE model with the linear equation of motion

$$\mathbf{M}\ddot{\mathbf{r}}(t) + \mathbf{D}_\zeta \dot{\mathbf{r}}(t) + (\mathbf{K}_e - F_x(t) \mathbf{K}_g) \mathbf{r}(t) = \mathbf{B}_{u,0} \mathbf{u}_b(t) + \mathbf{B}_{d,0} \mathbf{d}(t) \quad (1)$$

which was first derived in [12]. The beam-column is discretized by 32 and both axial extensions by one single one-dimensional EULER-BERNOULLI beam elements resulting in 34 finite elements with 35 nodes. The $[140 \times 1]$ FE displacement vector $\mathbf{r}(t)$ for 35 nodes contains two translational and two rotational displacements in and around y - and z -direction for each node. The left side of (1), which is derived in the following, represents the free lateral beam-column dynamics.

3.1.1 FE mass matrix \mathbf{M}

The distributed mass of the beam-column and the axial extensions are included in the $[140 \times 140]$ FE mass matrix \mathbf{M} . In addition, a discrete sensor mass $m_s = 7$ g that represents the strain gauges with cables are added to the lateral degrees of freedom of the central FE node 18 at $x = x_s$, see figure 1a.

3.1.2 FE damping matrix \mathbf{D}_ζ

Damping is assumed by RAYLEIGH proportional damping with the $[140 \times 140]$ FE damping matrix $\mathbf{D}_\zeta = \alpha \mathbf{M} + \beta \mathbf{K}_e$. The proportional damping coefficients α and β are obtained experimentally by the identified modal damping ratios $\zeta_1 = 6.3 \cdot 10^{-3}$ and $\zeta_3 = 6.2 \cdot 10^{-3}$ together with the angular eigenfrequencies ω_1 and ω_3 for the unloaded beam-column (10) for the first and third bending modes via

$$\begin{bmatrix} \alpha \\ \beta \end{bmatrix} = 2 \frac{\omega_1 \omega_3}{\omega_3^2 - \omega_1^2} \begin{bmatrix} \omega_3 & -\omega_1 \\ -1/\omega_3 & 1/\omega_1 \end{bmatrix} \begin{bmatrix} \zeta_1 \\ \zeta_3 \end{bmatrix}, \quad (2)$$

[16]. The first and third mode are chosen, since only the odd modes are observable with the chosen sensor position x_s in the beam-column center, figure 1.

3.1.3 FE stiffness matrix $\mathbf{K}_e - F_x(t) \mathbf{K}_g$

The FE stiffness matrix of the beam-column has two components, the elastic stiffness matrix \mathbf{K}_e and the geometric stiffness matrix \mathbf{K}_g , which describes the influence of the axial load $F_x(t)$ on the beam-column's lateral stiffness. The $[140 \times 140]$ stiffness matrices \mathbf{K}_e and \mathbf{K}_g contain the distributed stiffness of the beam-column and the axial extensions in figure 1a as well as discrete stiffness elements to describe the piezo-elastic support and sensor cable stiffness.

The axial load-dependent lateral and rotational stiffness $k_l(F_x)$ and $k_r(F_x)$ of the clamped elastic membrane springs are added to the entries for the lateral and rotational degrees of freedom of node 2 at $x = 0$ mm and node 34 at $x = l_b$ of the elastic and geometric stiffness matrices \mathbf{K}_e and \mathbf{K}_g . They are modeled linearly as

$$k_l(F_x) = k_{l,e} + F_x k_{l,g} \quad \text{and} \quad k_r(F_x) = k_{r,e} + F_x k_{r,g} \quad (3)$$

taking into account the experimentally observed stiffening effect of the elastic membrane spring's lateral and rotational stiffness with increasing axial load. The stiffness components are $k_{l,e} = 83.2 \cdot 10^3 \text{ N/mm}$ and $k_{r,e} = 499.4 \cdot 10^3 \text{ Nmm/rad}$ for the unloaded beam-column and $k_{l,g} = 22.1/\text{mm}$ and $k_{r,g} = 63.9 \text{ mm/rad}$ for the axial load proportional terms.

The mechanical stiffness $k_p = 29.5 \cdot 10^3 \text{ N/mm}$ of the short-circuited piezoelectric stack actuators is added to the lateral degrees of freedom in y - and z -direction of the first node 1 at $x = -l_{\text{ext}}$ and the last node 35 at $x = l_b + l_{\text{ext}}$ of the elastic stiffness matrix \mathbf{K}_e . Furthermore, a sensor cable stiffness $k_s = 6.2 \text{ N/mm}$ is added to the lateral degrees of freedom of the central FE node 18 at $x = x_s$.

The right side of (1) represents the external forces and disturbance bending moments acting on the beam-column.

3.1.4 FE external forces $\mathbf{B}_{u,0} \mathbf{u}_b(t)$

The actuator voltages $V_{p,y}(t)$ and $V_{p,z}(t)$ are simultaneously applied to both piezoelectric stack actuators in supports A and B in y - and z -direction. They are combined in the FE input vector

$$\mathbf{u}_b(t) = \begin{bmatrix} V_{p,y}(t) \\ V_{p,z}(t) \end{bmatrix}. \quad (4)$$

The $[140 \times 2]$ voltage input matrix

$$\mathbf{B}_{u,0} = \begin{bmatrix} \Theta & 0 & 0 & 0 & \dots & \Theta & 0 & 0 & 0 \\ 0 & \Theta & 0 & 0 & \dots & 0 & \Theta & 0 & 0 \end{bmatrix}^T \quad (5)$$

allocates the active forces of the piezoelectric stack actuators to the lateral degrees of freedom of the first node 1 at $x = -l_{\text{ext}}$ and the last node 35 at $x = l_b + l_{\text{ext}}$ of the FE model. The parameter $\Theta = 5.0 \text{ N/V}$ describes the active forces generated by the piezoelectric stack actuators for an applied voltage $V_{p,y/z}$.

3.1.5 FE disturbance bending moments $\mathbf{B}_{d,0} \mathbf{d}(t)$

To account for imperfections such as predeformation, eccentric loading or clamping moments that are present in real beam-column systems, [1], the disturbance bending moments

$$\mathbf{d}(t) = \begin{bmatrix} M_{d,y}(t) \\ M_{d,z}(t) \end{bmatrix} \quad (6)$$

are applied at the beam-column ends at $x = 0 \text{ mm}$ and $x = l_b$, figure 1a. The $[140 \times 2]$ disturbance input matrix

$$\mathbf{B}_{d,0} = \begin{bmatrix} 0 & 0 & 0 & 0 & 0 & 0 & 0 & 1 & 0 & \dots & 0 & 0 & -1 & 0 & 0 & 0 & 0 \\ 0 & 0 & 0 & 0 & 0 & 0 & -1 & 0 & 0 & \dots & 0 & 1 & 0 & 0 & 0 & 0 & 0 \end{bmatrix}^T \quad (7)$$

allocates the disturbance bending moments to the rotational degrees of freedom of node 2 at $x = 0 \text{ mm}$ and node 34 at $x = l_b$ in y - and z -direction.

3.1.6 FE measurement output

The beam-column bending strains at sensor position x_s in y - and z -direction according to figure 1a are used as the measurement output

$$\mathbf{y}_b(t) = \begin{bmatrix} \varepsilon_{s,y}(t) \\ \varepsilon_{s,z}(t) \end{bmatrix} \quad (8)$$

that is calculated from the FE displacement vector $\mathbf{r}(t)$ by the output equation

$$\mathbf{y}_b(t) = \mathbf{C}_{y,0} \mathbf{r}(t). \quad (9)$$

with the $[2 \times 140]$ output matrix $\mathbf{C}_{y,0}$ derived in [12]. The equation of motion (1) and the output equation (9) represent the full FE model of the beam-column.

3.2 REDUCED MODAL MODEL OF BEAM-COLUMN SYSTEM

Equation (1) describes the axial load-dependent lateral beam-column dynamics with 140 degrees of freedom. However, the relatively high order of the FE model for this simple beam-column system is unsuitable for model-based controller synthesis, so a model order reduction seems appropriate. Fortunately, only the first lateral beam-column mode of vibration is relevant to active buckling control, since it becomes unstable for axial loads greater than the first critical buckling load. Therefore, the FE model is modally decoupled and reduced by truncation to only include the first lateral mode of vibration for both y - and z -direction for controller design. Thus, the controller complexity is reduced considerably and the resulting modal beam-column model is observable and controllable with the given locations of the sensors and actuators, [17]. By solution of the modal eigenvalue problem

$$[(\mathbf{K}_e - F_x \mathbf{K}_g) - \omega^2 \mathbf{M}] \hat{\mathbf{r}} = 0, \quad (10)$$

the axial load-dependent eigenvectors $\hat{\mathbf{r}}(F_x)$ and angular eigenfrequencies $\omega(F_x) = 2\pi \cdot f(F_x)$, which are needed for decoupling, are obtained. The FE model is decoupled with the $[4N \times 2]$ modal matrix Φ that includes the two $[4N \times 1]$ eigenvectors $\hat{\mathbf{r}}_{1,y}(F_{x,m})$ and $\hat{\mathbf{r}}_{1,z}(F_{x,m})$ in y - and z - direction, [16]. These two eigenvectors are obtained for the constant axial load $F_{x,m} = 2500\text{N}$, which is in the middle of the test setup operational range $F_{x,\min} \leq F_x(t) \leq F_{x,\max}$ of the axial loads and provides good decoupling for all investigated axial loads, section 2. The linear approximation of the FE displacement vector by the $[2 \times 1]$ modal displacement vector $\mathbf{q}(t)$ is given by

$$\mathbf{r}(t) \approx \Phi \mathbf{q}(t) = \begin{bmatrix} \hat{\mathbf{r}}_{1,y}(F_{x,m}) & \hat{\mathbf{r}}_{1,z}(F_{x,m}) \end{bmatrix} \begin{bmatrix} q_{1,y}(t) \\ q_{1,z}(t) \end{bmatrix}. \quad (11)$$

3.2.1 Modal equation of motion

Inserting (11) in (1) and left-multiplication by Φ^T results in the modal equation of motion

$$\mathbf{M}_m \ddot{\mathbf{q}}(t) + \mathbf{D}_{\zeta,m} \dot{\mathbf{q}}(t) + (\mathbf{K}_{e,m} - F_x(t) \mathbf{K}_{g,m}) \mathbf{q}(t) = \mathbf{B}_{u,m} \mathbf{u}_b(t) + \mathbf{B}_{d,m} \mathbf{d}(t), \quad (12)$$

with the decoupled $[2 \times 2]$ modal mass matrix \mathbf{M}_m , modal damping matrix $\mathbf{D}_{\zeta,m}$, modal elastic stiffness matrix $\mathbf{K}_{e,m}$ and modal geometric stiffness matrix $\mathbf{K}_{g,m}$

$$\mathbf{M}_m = \Phi^T \mathbf{M} \Phi, \quad \mathbf{D}_{\zeta,m} = \Phi^T \mathbf{D}_{\zeta} \Phi, \quad \mathbf{K}_{e,m} = \Phi^T \mathbf{K}_e \Phi \quad \text{and} \quad \mathbf{K}_{g,m} = \Phi^T \mathbf{K}_g \Phi \quad (13)$$

as well as the decoupled $[2 \times 2]$ modal input matrices for the external forces and disturbance bending moments

$$\mathbf{B}_{u,m} = \Phi^T \mathbf{B}_{u,0} \quad \text{and} \quad \mathbf{B}_{d,m} = \Phi^T \mathbf{B}_{d,0}. \quad (14)$$

3.2.2 Modal output equation

Analog, the output equation (9) is decoupled and truncated by inserting (11). However, the truncation results in an underestimation of the static system response since the static contribution of the higher modes is neglected. Consequently, the static contribution of the higher modes is included in the output equation via the $[2 \times 2]$ modal feedthrough matrices for the actuator voltages

$$\mathbf{D}_{u,b} = \mathbf{C}_{y,0} [\mathbf{K}_e^{-1} - \Phi \mathbf{K}_{e,m} \Phi^T] \mathbf{B}_{u,0} \quad (15)$$

and the disturbance bending moments

$$\mathbf{D}_{d,m} = \mathbf{C}_{y,0} [\mathbf{K}_e^{-1} - \Phi \mathbf{K}_{e,m} \Phi^T] \mathbf{B}_{d,0}, \quad (16)$$

[16]. The resulting output equation of the reduced modal model is

$$\mathbf{y}_b(t) = \mathbf{C}_{y,m} \mathbf{q}(t) + \mathbf{D}_{u,b} \mathbf{u}_b(t) + \mathbf{D}_{d,b} \mathbf{d}(t), \quad (17)$$

with the decoupled $[2 \times 2]$ modal output matrix

$$\mathbf{C}_{y,m} = \mathbf{C}_{y,0} \Phi. \quad (18)$$

3.2.3 State space model of beam-column

Equations (12) and (17) represent the reduced modal model of the beam-column with piezo-elastic supports. For convenience, they are written in state space representation using the $[4 \times 1]$ modal state vector with modal displacements and velocities $\mathbf{x}_b(t) = [\mathbf{q}^T(t), \dot{\mathbf{q}}^T(t)]^T$. The modal state space equations of first order and the output equation are

$$\begin{aligned} \dot{\mathbf{x}}_b(t) &= \underbrace{\begin{bmatrix} \mathbf{0} & \mathbf{I} \\ -\mathbf{M}_m^{-1} (\mathbf{K}_{e,m} - F_x \mathbf{K}_{g,m}) & -\mathbf{M}_m^{-1} \mathbf{D}_{\zeta,m} \end{bmatrix}}_{[4 \times 4]} \mathbf{x}_b(t) + \underbrace{\begin{bmatrix} \mathbf{0} \\ \mathbf{M}_m^{-1} \mathbf{B}_{u,m} \end{bmatrix}}_{[4 \times 2]} \mathbf{u}_b(t) + \underbrace{\begin{bmatrix} \mathbf{0} \\ \mathbf{M}_m^{-1} \mathbf{B}_{d,m} \end{bmatrix}}_{[4 \times 2]} \mathbf{d}(t) \\ \mathbf{y}_b(t) &= \underbrace{\begin{bmatrix} \mathbf{C}_{y,m} & \mathbf{0} \end{bmatrix}}_{[2 \times 4]} \mathbf{x}_b(t) + \underbrace{\mathbf{D}_{u,b}}_{[2 \times 2]} \mathbf{u}_b(t) + \underbrace{\mathbf{D}_{d,b}}_{[2 \times 2]} \mathbf{d}(t) \end{aligned} \quad (19)$$

with zero and identity matrices $\mathbf{0}$ and \mathbf{I} of appropriate dimensions, [17].

3.2.4 Transfer function of modal beam-column model

After LAPLACE transformation, the state space realization of the modal beam-column model (19) is

$$\begin{aligned} s \mathbf{x}_b(s) &= \mathbf{A}_b(F_x) \mathbf{x}_b(s) + \mathbf{B}_{u,b} \mathbf{u}_b(s) + \mathbf{B}_{d,b} \mathbf{d}(s) \\ \mathbf{y}_b(s) &= \mathbf{C}_{y,b} \mathbf{x}_b(s) + \mathbf{D}_{u,b} \mathbf{u}_b(s) + \mathbf{D}_{d,b} \mathbf{d}(s), \end{aligned} \quad (20)$$

[18]. The influence of axial load $F_x(t)$ on the beam-column is included in system matrix $\mathbf{A}_b(F_x)$. The $[2 \times 2]$ matrix of transfer functions of actuator voltages (4) to beam-column strains (8) is obtained from (20) according to

$$\mathbf{G}_b(F_x, s) = \frac{\mathbf{y}_b(s)}{\mathbf{u}_b(s)} = \mathbf{C}_{y,b} (\mathbf{I}s - \mathbf{A}_b(F_x))^{-1} \mathbf{B}_{u,b} + \mathbf{D}_{u,b} \stackrel{s}{=} \left[\begin{array}{c|c} \mathbf{A}_b(F_x) & \mathbf{B}_{u,b} \\ \hline \mathbf{C}_{y,b} & \mathbf{D}_{u,b} \end{array} \right] \quad (21)$$

where the last part of (21) is a short notation for the transfer function of the four state space matrices $\mathbf{A}_b(F_x)$, $\mathbf{B}_{u,b}$, $\mathbf{C}_{y,b}$ and $\mathbf{D}_{u,b}$, [19].

3.3 BEAM-COLUMN PLANT WITH ELECTRICAL COMPONENTS

The real beam-column is embedded in an experimental test setup with additional electrical components used for signal conditioning, section 2. For controller synthesis, a beam-column plant is needed that properly describes the dynamic behavior of the beam-column (21) with electrical components via the transfer function of the control input

$$\mathbf{u}(s) = \begin{bmatrix} u_y(s) \\ u_z(s) \end{bmatrix} \quad (22)$$

to measurement output

$$\mathbf{y}(s) = \begin{bmatrix} y_y(s) \\ y_z(s) \end{bmatrix}. \quad (23)$$

Therefore, the beam-column transfer function is extended by transfer functions for the reconstruction filters $\mathbf{G}_{rf}(s)$, piezo amplifiers $\mathbf{G}_{pa}(s)$, strain gauge amplifiers $\mathbf{G}_{sg}(s)$ and the real-time platform $\mathbf{G}_{rt}(s)$. Figure 4 shows the block diagram of the extended beam-column plant.

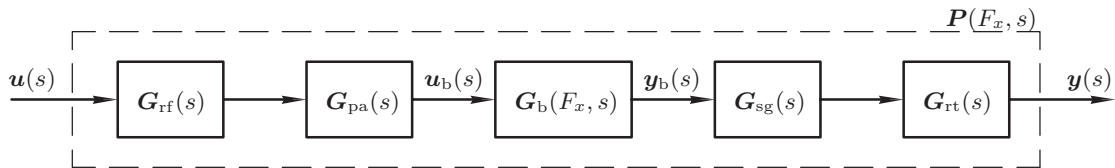


Fig. 4 Block diagram of the beam-column plant with electrical components

To generate the actuator voltages (4), the control input (22) is filtered by analog low-pass reconstruction filters (rf) and amplified by piezo amplifiers (pa)

$$\mathbf{u}_b(s) = \mathbf{G}_{pa}(s) \mathbf{G}_{rf}(s) \mathbf{u}(s). \quad (24)$$

The reconstruction filters $\mathbf{G}_{rf}(s)$ are analog 6-th order elliptic low-pass filters with cutoff frequency at 2200 Hz that are used to smooth the control input. In the considered frequency range, the piezo amplifiers $\mathbf{G}_{pa}(s)$ can be modeled with a constant gain of 30 with adequate accuracy. The measurement outputs (23) are the beam-column surface strains (8), which are amplified and filtered by strain gauge amplifiers (sg) and converted into a digital signal in the real-time platform (rt)

$$\mathbf{y}(s) = \mathbf{G}_{rt}(s) \mathbf{G}_{sg}(s) \mathbf{y}_b(s). \quad (25)$$

The strain gauge amplifiers $\mathbf{G}_{sg}(s)$ amplify the strain signals by a factor of $2.0 \cdot 10^4$ with an integrated analog 7-th order Butterworth low-pass filter using a cutoff frequency of 2000 Hz. Finally, the A/D-conversion in the real-time platform $\mathbf{G}_{rt}(s)$ with a sampling frequency of 5000 Hz leads to a time-delay or, respectively, phase shift that is modeled by a 2nd order Padé approximation of 1.5 samples, [19].

The complete beam-column plant with the electrical components shown in figure 4 is given by the $[2 \times 2]$ transfer function matrix

$$\mathbf{P}(F_x, s) = \frac{\mathbf{y}(s)}{\mathbf{u}(s)} = \mathbf{G}_{rt}(s) \mathbf{G}_{sg}(s) \mathbf{G}_b(F_x, s) \mathbf{G}_{pa}(s) \mathbf{G}_{rf}(s) = \begin{bmatrix} P_y(F_x, s) & 0 \\ 0 & P_z(F_x, s) \end{bmatrix} \quad (26)$$

as a series connection of the individual transfer functions. For the later controller synthesis in section 4, the beam-column plant can again be written in form of the state space matrices

$$\mathbf{P}(F_x, s) \stackrel{s}{=} \left[\begin{array}{c|c} \mathbf{A}(F_x) & \mathbf{B}_u \\ \hline \mathbf{C}_y & \mathbf{0} \end{array} \right]. \quad (27)$$

The system matrix beam-column plant with the electrical components

$$\mathbf{A}(F_x) = \mathbf{A}_e + F_x \mathbf{A}_g. \quad (28)$$

depends linearly on the axial load F_x that, in the real experimental test setup, is physically limited by $F_{x,\min} \leq F_x(t) \leq F_{x,\max}$, section 2. The vertices of the system matrix (28) are defined for the extreme values of the axial load as $[\mathbf{A}(F_{x,\min}), \mathbf{A}(F_{x,\max})]$. Thus, the beam-column plant (27) represents the class of polytopic LPV systems, [20].

3.4 COMPARISON OF NUMERICAL AND EXPERIMENTAL DYNAMIC BEHAVIOR

In the following, the dynamic transfer behavior of the beam-column plant (26) is compared with experimental data to show that the derived model appropriately describes the real beam-column system. The parameters of the mathematical model presented in section 2 are determined by calibration with a least-square error minimization. For zero initial conditions and the conversion $s = j\Omega$, the two transfer functions from (26)

$$P_y(F_x, \Omega) = \frac{y_y(\Omega)}{u_y(\Omega)} \quad \text{and} \quad P_z(F_x, \Omega) = \frac{y_z(\Omega)}{u_z(\Omega)} \quad (29)$$

represent the measurement output $y_{y/z}$ in y - and z -direction (23) for a harmonic excitation of real-time output $u_{y/z}$ in y - and z -direction (22) with excitation angular frequency Ω , [18]. In the mathematical model, both y - and z -direction are assumed to be identical.

Figure 5a shows the amplitude $|P_{y/z}(F_x)|$ and phase responses $\arg P_{y/z}(F_x)$ of (29) for the beam-column loaded with static axial loads $F_x = 337$ N, 2500 N and 3000 N for model and experiment. $F_{x,\min} = 337$ N is the minimum axial load of the experimental test setup, $F_{x,m} = 2500$ N is the axial load used for the modal decoupling of the FE model (11) and $F_x = 3000$ N is the maximum axial load the transfer function of the uncontrolled beam-column can be measured due to otherwise too high static deformations.

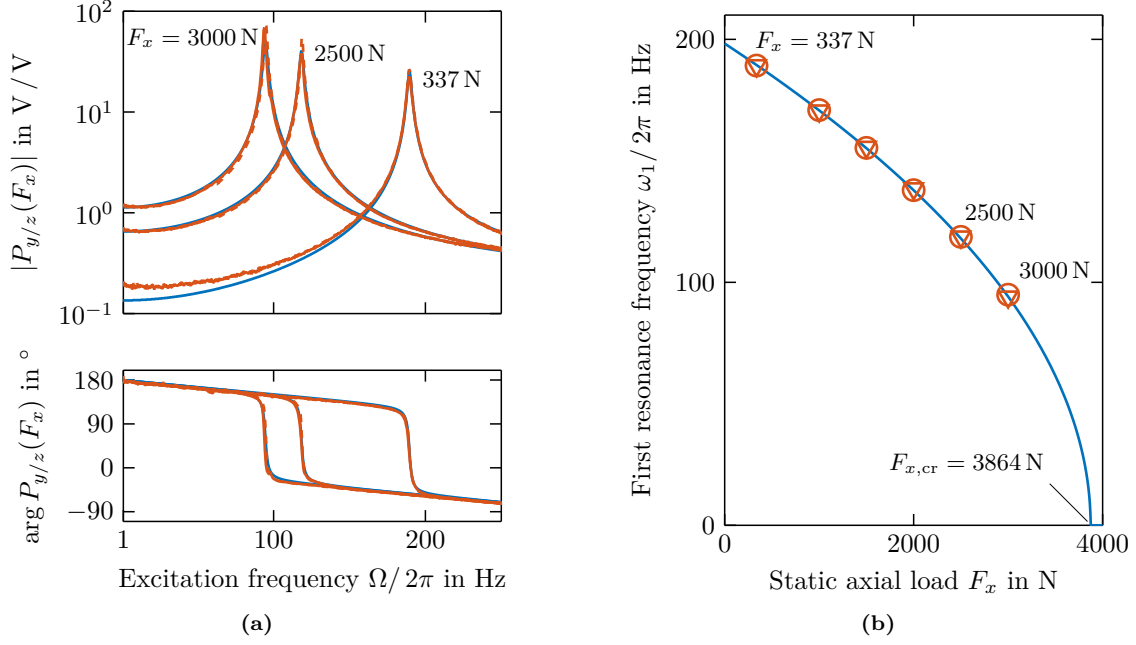


Fig. 5 Comparison of numerical and experimental beam-column dynamic behavior, (a) amplitude $|P_{y/z}(F_x)|$ and phase $\arg P_{y/z}(F_x)$ for static axial loads $F_x = 337$ N, 2500 N and 3000 N from numerical simulation (—) and experiment in y -direction (—) and z -direction (---), (b) first resonance frequency $\omega_1(F_x)/2\pi$ for varying axial load $0 \text{ N} \leq F_x \leq 4000$ N from simulation (—) and $337 \text{ N} \leq F_x \leq 3000$ N from experiments in y -direction (∇) and z -direction (\circ)

Amplitude and phase responses in y - and z -direction from model (29) and experiment coincide well for the considered frequency range of $0 \text{ Hz} < \Omega/2\pi < 250$ Hz. The first resonance frequencies $\omega_1(F_x)/2\pi$ for the three displayed axial loads at 190 Hz, 119 Hz and 95 Hz match for numerical simulation and experiment. The resonance frequencies correspond to the maxima $\max(|P_{y/z}(F_x)|) = |P_{y/z}(F_x, \Omega = \omega_1)|$ of the amplitude responses. Furthermore, the static system response $|P_{y/z}(F_x, \Omega \rightarrow 0)|$ for higher axial loads is well described by the one mode modal beam-column model (21) with static correction of higher modes (15). For $F_x = 337$ N, the model underestimates the static response since the model is calibrated rather for higher axial loads, which are more important for the active buckling control. In the frequency range up to 250 Hz, the electrical components mainly contribute to the dynamic behavior by a phase shift that is well captured by the model.

Figure 5b shows the decrease of the first resonance frequency $\omega_1(F_x)/2\pi$ due to increasing static axial load in the experiment for designated axial loads between $337 \text{ N} \leq F_x \leq 3000$ N and for the numerical simulation from $0 \text{ N} \leq F_x \leq 4000$ N. In the numerical simulation, the first resonance frequency $\omega_1(F_x)/2\pi$ is calculated by solution of the well-known eigenvalue problem

$$\det [(\mathbf{K}_{e,m} - F_x \mathbf{K}_{g,m}) - \omega_1^2 \mathbf{M}_m] = 0. \quad (30)$$

As seen in figure 5b, the model (26) agrees well with the experimentally measured resonance frequencies. In the numerical simulation, the first resonance frequency reaches zero for the critical buckling load that can, therefore, be calculated from the modal elastic and geometric stiffness matrices by solution of the modified eigenvalue problem (30) for $\omega_1 = 0$ by

$$\det [\mathbf{K}_{e,m} - F_{x,cr} \mathbf{K}_{g,m}] = 0, \quad (31)$$

[21]. For the given boundary conditions, the critical buckling load for the first mode is $F_{x,cr} = 3864$ N. The comparison with experimental data shows that the LPV beam-column plant (26) appropriately describes the axial load-dependent lateral beam-column dynamic behavior. Thus, the model-based gain-scheduled \mathcal{H}_∞ control approach that is presented in the following section appears to be promising.

4 GAIN-SCHEDULED \mathcal{H}_∞ BUCKLING CONTROL

In this section, the gain-scheduled \mathcal{H}_∞ buckling control, which is based on the mathematical model of the beam-column and, as the model, is identical in y - and z -direction, is presented. As can be seen from (27), the beam-column plant is described by a parameter-dependent LPV system in which the system matrix $\mathbf{A}(F_x)$ depends linearly on the axial load F_x and becomes unstable for the critical buckling load $F_{x,\text{cr}}$, figure 5b. For these types of systems, gain-scheduled \mathcal{H}_∞ control is an appropriate control approach since it incorporates the axial load-dependency and guarantees stability and robust performance for the entire range of operation, [22–24].

The parameter-dependent state space model of the beam-column plant (27) with the control input $\mathbf{u}(s)$ (22) and measurement output $\mathbf{y}(s)$ (23) is extended by additional exogenous inputs $\mathbf{w}(s)$ (38) and performance outputs $\mathbf{z}(s)$ (42), which are used to get access to all relevant system parameters for control. The extended open-loop plant $\mathbf{P}_{\text{ol}}(F_x, s)$ describes the relation of performance outputs $\mathbf{z}(s)$ and measurement output $\mathbf{y}(s)$ to exogenous inputs $\mathbf{w}(s)$ and control input $\mathbf{u}(s)$ via

$$\begin{bmatrix} \mathbf{z}(s) \\ \mathbf{y}(s) \end{bmatrix} = \mathbf{P}_{\text{ol}}(F_x, s) \begin{bmatrix} \mathbf{w}(s) \\ \mathbf{u}(s) \end{bmatrix}, \quad (32)$$

which is the general form of the open-loop plant used for gain-scheduled \mathcal{H}_∞ control, [25]. The open-loop plant and its inputs and outputs are derived in detail in section 4.1. Figure 6 shows the extended open-loop plant in standard control configuration, [19].

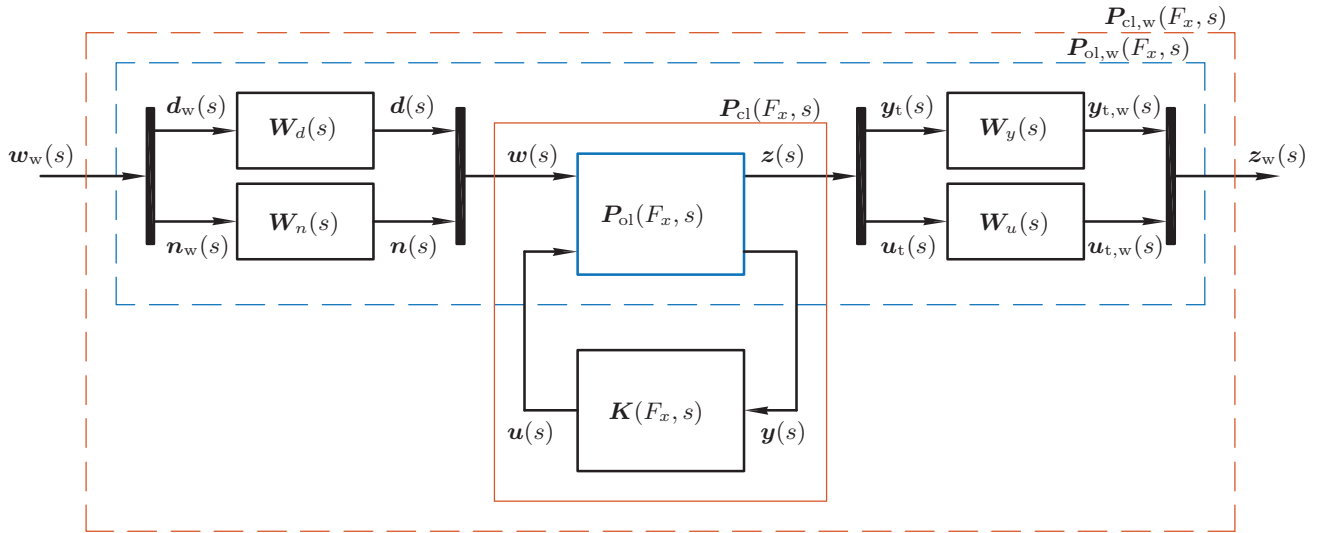


Fig. 6 Gain-scheduled \mathcal{H}_∞ block diagram in standard control configuration: open-loop plant $\mathbf{P}_{\text{ol}}(F_x, s)$ (—), closed-loop plant $\mathbf{P}_{\text{cl}}(F_x, s)$ (—), weighted open-loop plant $\mathbf{P}_{\text{ol},w}(F_x, s)$ (—), and weighted closed-loop plant $\mathbf{P}_{\text{cl},w}(F_x, s)$ (—)

The dynamic, axial load-dependent controller $\mathbf{K}(F_x, s)$ connects the measurement output (23) with the control input (22) of the open-loop plant (32) via

$$\mathbf{u}(s) = \mathbf{K}(F_x, s) \mathbf{y}(s). \quad (33)$$

The open-loop plant with the control feedback (33) leads to the closed-loop plant

$$\mathbf{P}_{\text{cl}}(F_x, s) = \frac{\mathbf{z}(s)}{\mathbf{w}(s)} = \mathcal{F}_1(\mathbf{P}_{\text{ol}}(F_x, s), \mathbf{K}(F_x, s)) \quad (34)$$

with exogenous inputs $\mathbf{w}(s)$ and performance outputs $\mathbf{z}(s)$, which is obtained by the lower linear fractional transformation (LFT) \mathcal{F}_1 of the open-loop plant and the dynamic controller, [19, 25].

In order to tune the system dynamics of the closed-loop beam-column plant and to achieve the desired controller performance in the frequency range of interest, the open-loop plant in (32) is extended by the frequency-dependent weights $\mathbf{W}_d(s)$, $\mathbf{W}_n(s)$, $\mathbf{W}_y(s)$ and $\mathbf{W}_u(s)$. The choice and design of the weights is presented in section 4.2. The open-loop plant (37) with additional input and output weights results in the weighted open-loop plant $\mathbf{P}_{ol,w}(F_x, s)$, figure 6, with

$$\begin{bmatrix} \mathbf{z}_w(s) \\ \mathbf{y}(s) \end{bmatrix} = \mathbf{P}_{ol,w}(F_x, s) \begin{bmatrix} \mathbf{w}_w(s) \\ \mathbf{u}(s) \end{bmatrix}. \quad (35)$$

The lower LFT of the weighted open-loop plant (35) and the control feedback (33) leads to the weighted closed-loop plant

$$\mathbf{P}_{cl,w}(F_x, s) = \frac{\mathbf{z}_w(s)}{\mathbf{w}_w(s)} = \mathcal{F}_l(\mathbf{P}_{ol,w}(F_x, s), \mathbf{K}(F_x, s)) \quad (36)$$

that describes the relation of the weighted exogenous inputs $\mathbf{w}_w(s)$ to the weighted performance outputs $\mathbf{z}_w(s)$. The synthesis of the gain-scheduled \mathcal{H}_∞ controller based on (36) is presented in section 4.3.

Finally, the controller performance is numerically verified by the dynamic behavior of the closed-loop beam-column plant in section 4.4.

4.1 OPEN-LOOP PLANT

In the following, the open-loop plant and the inputs and outputs in (32) will be derived. The parameter-dependent state space model of the beam-column plant (27) is extended by an extra column for exogenous inputs $\mathbf{w}(s)$ (38) and an extra row for performance outputs $\mathbf{z}(s)$ (42) leading to the open-loop plant

$$\mathbf{P}_{ol}(F_x, s) \doteq \left[\begin{array}{c|cc} \mathbf{A}(F_x) & \mathbf{B}_w & \mathbf{B}_u \\ \hline \mathbf{C}_z & \mathbf{0} & \mathbf{D}_z \\ \mathbf{C}_y & \mathbf{D}_y & \mathbf{0} \end{array} \right]. \quad (37)$$

In (32), the exogenous input vector

$$\mathbf{w}(s) = \begin{bmatrix} \mathbf{d}(s) \\ \mathbf{n}(s) \end{bmatrix} \quad (38)$$

contains the disturbance bending moments (6) and additional measurement noise $\mathbf{n}(s) = [n_y(s), n_z(s)]^T$ that is added to the measurement output (23). Thus, the modified measurement output equation is

$$\mathbf{y}(s) = \mathbf{C}_y \mathbf{x}(s) + \mathbf{n}(s) = \mathbf{C}_y \mathbf{x}(s) + \mathbf{D}_y \mathbf{w}(s), \quad (39)$$

with measurement feedthrough matrix

$$\mathbf{D}_y = \begin{bmatrix} \mathbf{0} & \mathbf{I} \end{bmatrix}. \quad (40)$$

The input matrix \mathbf{B}_w in (37) contains the disturbance input matrix $\mathbf{B}_{d,b}$ from (20) with additional zero entries to fit the extended plant dimensions.

The performance outputs are chosen in order to reduce lateral deformation and vibration of the beam-column and to limit the control signals. They are chosen as the measurement output without measurement noise and the control input (22)

$$\mathbf{y}_t(s) = \mathbf{C}_y \mathbf{x}(s) \quad \text{and} \quad \mathbf{u}_t(s) = \mathbf{I} \mathbf{u}(s). \quad (41)$$

In (32), they are combined in the performance output vector

$$\mathbf{z}(s) = \begin{bmatrix} \mathbf{y}_t(s) \\ \mathbf{u}_t(s) \end{bmatrix} = \mathbf{C}_z \mathbf{x}(s) + \mathbf{D}_z \mathbf{u}(s) \quad (42)$$

with performance output and feedthrough matrices

$$\mathbf{C}_z = \begin{bmatrix} \mathbf{C}_y \\ \mathbf{0} \end{bmatrix} \quad \text{and} \quad \mathbf{D}_z = \begin{bmatrix} \mathbf{0} \\ \mathbf{I} \end{bmatrix}. \quad (43)$$

4.2 WEIGHTED OPEN-LOOP PLANT

In the previous section, the exogenous inputs (38) and performance outputs (42) were defined for the open-loop system. In order to properly tune the gain-scheduled \mathcal{H}_∞ controller for active buckling control, frequency-dependent input and output weights are added to the open-loop system (37), figure 6. The weighted exogenous inputs and weighted performance outputs are given by

$$\mathbf{w}_w(s) = \begin{bmatrix} \mathbf{W}_d^{-1}(s) & \mathbf{0} \\ \mathbf{0} & \mathbf{W}_n^{-1}(s) \end{bmatrix} \mathbf{w}(s) \quad \text{and} \quad \mathbf{z}_w(s) = \begin{bmatrix} \mathbf{W}_y(s) & \mathbf{0} \\ \mathbf{0} & \mathbf{W}_u(s) \end{bmatrix} \mathbf{z}(s) \quad (44)$$

leading to the weighted open-loop plant (35). The $[2 \times 2]$ input weight matrices for the disturbance bending moments $\mathbf{W}_d(s) = \text{diag}(W_d(s), W_d(s))$ and the measurement noise $\mathbf{W}_n(s) = \text{diag}(W_n(s), W_n(s))$ are chosen as diagonal matrices with scalar transfer functions. In the same way, the $[2 \times 2]$ output weight matrices $\mathbf{W}_y(s) = \text{diag}(W_y(s), W_y(s))$ and $\mathbf{W}_u(s) = \text{diag}(W_u(s), W_u(s))$ are obtained for the performance outputs.

The dynamics of the closed-loop plant (36) are influenced by the input and output weights. A stronger weight increases the influence of an input or output in the controller synthesis for the specified frequency range. The weights are selected as simple as possible in order to keep the controller order low. The actual weight parameters are then tuned iteratively by hand to achieve satisfactory closed-loop control performance, see section 4.4, [25]. Constant weights are chosen for the disturbance bending moments and the control input as

$$W_d(s) = 2.2 \text{ Nmm} \quad \text{and} \quad W_u(s) = 1 \text{ V}^{-1}. \quad (45)$$

The measurement output and measurement noise are modified by frequency-dependent weights of the general form

$$W(s) = \left(\frac{b^{-1/p} s + \omega_c}{s + \omega_c a^{1/p}} \right)^p, \quad (46)$$

[19]. In (46), the parameter a sets the filter amplitude for low frequencies, b sets the filter amplitude for high frequencies, ω_c is the filter cutoff frequency and p is the filter order. $W_y(s)$ is chosen as a first order low-pass filter with a small value of a to approximate an integral term that is necessary to achieve stationary accuracy in spite of constant imperfections that counteract the active stabilization, [25]. $W_n(s)$ is chosen as a fourth order high-pass filter that ensures low noise amplification at high frequencies outside the frequency range of interest. The higher filter order results in a sharper decrease of the transfer function that is needed for the separation from the higher beam-column modes. The parameters of the frequency-dependent weights are summarized in table 1.

weight	a	b	p	ω_c
W_n	1600 V ⁻¹	1/75 V ⁻¹	4	400 · 2π rad/s
W_y	1/1000 V	5 V	1	400 · 2π rad/s

Tab. 1 Parameters of frequency-dependent input and output weights

4.3 CONTROLLER SYNTHESIS

In the following, the synthesis of the dynamic and parameter-dependent controller $\mathbf{K}(F_x, s)$ is presented. The controller is equally dependent on axial load F_x as the underlying open-loop plant (37) and is described by the transfer function

$$\mathbf{K}(F_x, s) \stackrel{s}{=} \left[\begin{array}{c|c} \mathbf{A}_c(F_x) & \mathbf{B}_c(F_x) \\ \mathbf{C}_c(F_x) & \mathbf{D}_c(F_x) \end{array} \right] \quad (47)$$

in LAPLACE domain. In the experiment, $\mathbf{K}(F_x, s)$ is determined in real-time from the measured axial load $F_x(t)$ via the axial load-dependent controller state space matrices

$$\begin{aligned} \mathbf{A}_c(F_x) &= \mathbf{A}_{e,c} + F_x \mathbf{A}_{g,c}, & \mathbf{B}_c(F_x) &= \mathbf{B}_{e,c} + F_x \mathbf{B}_{g,c}, \\ \mathbf{C}_c(F_x) &= \mathbf{C}_{e,c} + F_x \mathbf{C}_{g,c} & \text{and} & \mathbf{D}_c(F_x) = \mathbf{D}_{e,c} + F_x \mathbf{D}_{g,c}. \end{aligned} \quad (48)$$

The goal of the gain-scheduled \mathcal{H}_∞ control is to minimize the induced \mathcal{L}_2 -norm of the weighted closed-loop plant (36) below γ for arbitrary trajectories of the variable parameter vector $F_x(t)$

$$\| \mathbf{P}_{cl,w}(F_x, s) \|_{\mathcal{L}_2} = \sup_{\mathbf{w} \neq 0} \frac{\| \mathbf{z}_w(s) \|_2}{\| \mathbf{w}_w(s) \|_2} \leq \gamma, \quad (49)$$

[22]. The weighted closed-loop plant (36) obtained by the lower LFT of the weighted open-loop plant (35) and the control feedback (33) is given by the transfer function of the closed-loop state space matrices

$$\mathbf{P}_{cl,w}(F_x, s) \stackrel{s}{=} \left[\begin{array}{c|c} \mathbf{A}_{cl}(F_x) & \mathbf{B}_{cl}(F_x) \\ \mathbf{C}_{cl}(F_x) & \mathbf{D}_{cl}(F_x) \end{array} \right]. \quad (50)$$

The closed-loop plant (50) is stable and has quadratic \mathcal{H}_∞ performance γ if there exists a positive definite matrix $\mathbf{X} \succ 0$ that satisfies the condition known as bounded real lemma

$$\mathcal{B}_{\mathbf{P}_{cl,w}(F_x)}(\mathbf{X}, \gamma) = \begin{bmatrix} \mathbf{A}_{cl}^T(F_x) \mathbf{X} + \mathbf{X} \mathbf{A}_{cl}(F_x) & \mathbf{X} \mathbf{B}_{cl}(F_x) & \mathbf{C}_{cl}^T(F_x) \\ \mathbf{B}_{cl}^T(F_x) \mathbf{X} & -\gamma \mathbf{I} & \mathbf{D}_{cl}^T(F_x) \\ \mathbf{C}_{cl}(F_x) & \mathbf{D}_{cl}(F_x) & -\gamma \mathbf{I} \end{bmatrix} \prec 0, \quad (51)$$

[22]. Equation (51) has to be solved for the vertices of the polytopic LPV system (50) resulting in two linear matrix inequalities (LMI). The vertices define the operation range of the gain-scheduled \mathcal{H}_∞ control that is defined by the minimum and maximum realizable axial loads $F_{x,\min} = 337$ N and $F_{x,\max} = 5000$ N of the experimental test setup, section 2. Consequently, the bounded real lemma (51) is solved simultaneously for the two weighted closed loop plants $\mathbf{P}_{cl,w}(F_{x,\min})$ and $\mathbf{P}_{cl,w}(F_{x,\max})$ which is done with the MATLAB® *Robust Control Toolbox*, [20].

4.4 NUMERICAL VERIFICATION OF CONTROLLER PERFORMANCE

The performance of the gain-scheduled \mathcal{H}_∞ buckling control is verified numerically prior to the application to the experimental test setup by comparing the passive open-loop and active closed-loop beam-column plant dynamic behavior. Figure 7 shows the amplitude responses of the open-loop beam-column plant (37) and closed loop beam-column plant (34) for the transfer path from disturbance bending moments \mathbf{d} to the performance output \mathbf{y}_t , figure 6, for zero initial conditions and the conversion $s = j\Omega$. As seen before in figure 5a, the resonance frequencies of the open-loop amplitude responses $P_{d \rightarrow y}(F_x, \Omega)$ decrease for increasing axial load F_x and the static response for $\Omega \rightarrow 0$ increases. For axial loads exceeding $F_x \geq F_{x,cr} = 3864$ N, the open-loop plant becomes unstable.

The closed-loop plant (34) is quadratically stable by solution of the bounded real lemma (51). The dynamic behavior is mainly determined by the frequency-dependent input and output weights (44), which were derived in section 4.2. For each transfer path from the inputs (38) to the outputs (42) of the closed-loop system, the input and output weights define the shape of the closed-loop amplitude responses. For the transfer path from disturbance bending moments \mathbf{d} to the performance output \mathbf{y}_t , an upper bound

$$\Gamma_{d \rightarrow y_t}(\Omega) = \frac{1}{|W_d(\Omega) W_y(\Omega)|} \quad (52)$$

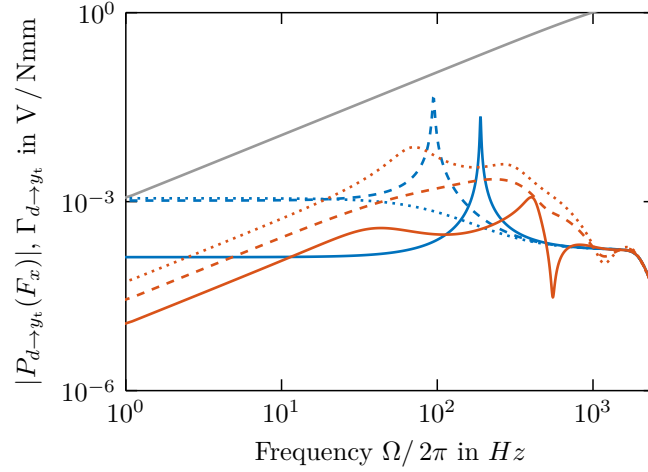


Fig. 7 Amplitude responses $|P_{d \rightarrow y_t}(F_x, \Omega)|$ for the open-loop plant at axial loads $F_x = 337$ N (—), 3000 N (---) and 5000 N (···) and the closed-loop plant at axial loads $F_x = 337$ N (—), 3000 N (---) and 5000 N (···) and frequency-dependent bound $\Gamma_{d \rightarrow y_t}(\Omega)$ (—)

limits the closed-loop dynamic behavior. For low frequencies, it reduces the amplitude response, thus creating an integral control as intended. Furthermore, the resonance amplitudes at the different axial loads F_x are reduced resulting in a reduction of lateral vibrations in the first lateral mode, see section 5.2.

5 EXPERIMENTAL RESULTS FOR ACTIVE BUCKLING CONTROL

In this section, experimental results of the axially loaded beam-column system with and without gain-scheduled \mathcal{H}_∞ buckling control or, respectively, active and passive configuration are presented. The experiments are conducted on the experimental test setup shown in figure 3 with ramp- and step-shaped time-varying axial load $F_x(t)$. The beam-column modal displacements $\mathbf{q}(t) = [q_{1,y}(t), q_{1,z}(t)]^T$ from (11) are plotted and compared for the passive and active configuration of the beam-column system. They are calculated from the beam-column surface strains (8) and the invertible $[2 \times 2]$ modal output matrix (18) via

$$\mathbf{q}(t) = \begin{bmatrix} q_{1,y}(t) \\ q_{1,z}(t) \end{bmatrix} = \mathbf{C}_{y,m}^{-1} \mathbf{y}_b(t). \quad (53)$$

First, the experimental results for the beam-column loaded by a ramp-shaped axial load $F_x(t)$ and then for a step-shaped axial load $F_x(t)$ are presented.

5.1 RAMP-SHAPED AXIAL LOADS

In the experimental test setup, the ramp-shaped axial load on the beam-column is generated by increasing the lever ratio of mass 5 of 30 kg on the hinged beam 6 in figure ???. This way, the ramp-shaped axial load $F_x(t)$ is increased continuously with a rate of approximately 20 N/s. The results of the beam-column system in passive and active configuration are shown in figure 8. The absolute value of the modal displacements $q_{1,y}$ and $q_{1,z}$ for the first modes in y - and z -direction are plotted with respect to the axial load F_x in figure 8a. Figure 8b shows the modal displacements $q_{1,y}$ and $q_{1,z}$ according to (53) in the y - and z -direction.

In the passive configuration, the load-displacement curve in figure 8a shows the typical continuous deformation with increasing axial load, which is known from real, imperfect beam-columns, [1]. Sudden buckling does not occur. In theory, the ideal beam-column with circular cross-section has infinite directions of buckling. The real, passive beam-column, however, deforms continuously in an angle of $\vartheta_p = 16^\circ$ measured from the positive y -direction, see figure 8b. The direction of buckling of the real uncontrolled system is mainly dependent on a random predeformation of the beam-column and the random assembly conditions of the test setup that vary accordingly. It is not possible to

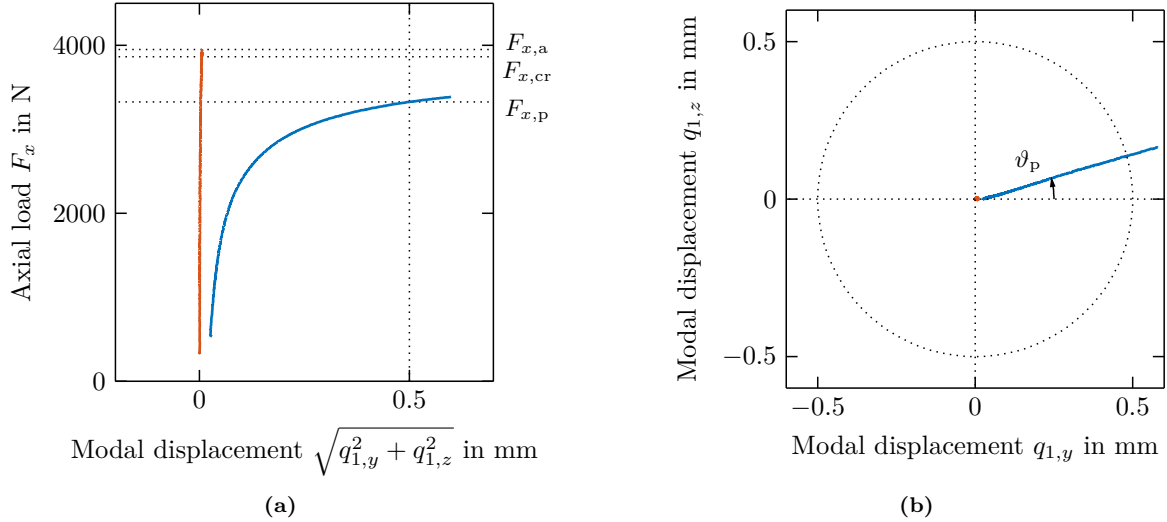


Fig. 8 Beam-column with ramp-shaped axial load $F_x(t)$ in passive (—) and active (—) configuration, (a) absolute modal displacement versus axial load F_x , (b) modal displacements $q_{1,y}$ and $q_{1,z}$ in y - and z -direction

detect one single critical buckling load of the uncontrolled system, only a maximum admissible deformation can be set depending on the intended application. Here, a maximum admissible deformation of 0.5 mm is defined to avoid plastic deformation of the beam-column. It is reached for an axial load of $F_{x,p} = 3325 \text{ N} = 0.86 F_{x,cr}$ which is considerably less than the theoretical critical buckling load $F_{x,cr} = 3864 \text{ N}$ determined from the FE model via (31).

In the active configuration, the piezoelectric stack actuators in the piezo-elastic supports cancel out the initial deformation of the beam-column and then keep the modal displacements close to 0 mm for the ramp-shaped axial load $F_x(t)$ contrary to the passive configuration, figure 8a. The gain-scheduled \mathcal{H}_∞ control is able to stabilize the beam-column up to an axial load of $F_{x,a} = 3950 \text{ N} = 1.02 F_{x,cr} = 1.19 F_{x,p}$. Up to $F_{x,a}$, the deformation in both y - and z -direction remains zero, figure 8b. At $F_{x,a}$, the experiment for the active case is stopped since the voltage saturation of the piezoelectric stack actuators is reached.

5.2 STEP-SHAPED AXIAL LOADS

In the experimental test setup, the step-shaped axial load on the beam-column is generated by releasing the weight 10 of 7.5 kg by the electromagnet 11 in figure ???. The course of the axial load $F_x(t)$ in the experimental test setup that is measured with load cell 12 is plotted over time for the passive and active configuration of the beam-column in figure 9a. The application of $F_x(t)$ in the experimental test setup is influenced by the inertia of the test setup mass and is the same for the passive and active configuration. Before the step load is applied at time $t_{\text{step}} = 0.27 \text{ s}$, the initial axial load is $F_x(t \leq t_{\text{step}}) = 1500 \text{ N}$. The maximum axial load is $F_x(t \approx 0.3 \text{ s}) = 2600 \text{ N}$ and, after the dynamic effects of the test setup have decayed, the axial load is $F_x(t \geq 1.5 \text{ s}) = 2050 \text{ N}$.

Figure 9b shows the modal displacement $q_{1,y}$ in y -direction over time in response to the step-shaped axial load from figure 9a for the passive and active configuration of the beam-column. Table 2 shows the values of the modal beam-column displacements before application of the step load, $t \leq t_{\text{step}}$, for the maximum displacements at $t \approx 0.3 \text{ s}$, and after application of the step load, $t > 1.5 \text{ s}$.

$q_{1,y}$ in mm	$t \leq t_{\text{step}}$	$t \approx 0.3 \text{ s}$	$t > 1.5 \text{ s}$
passive	0.039	0.134	0.067
active	0.001	0.027	0.001

Tab. 2 Beam-column modal displacements for step-shaped axial load $F_x(t)$

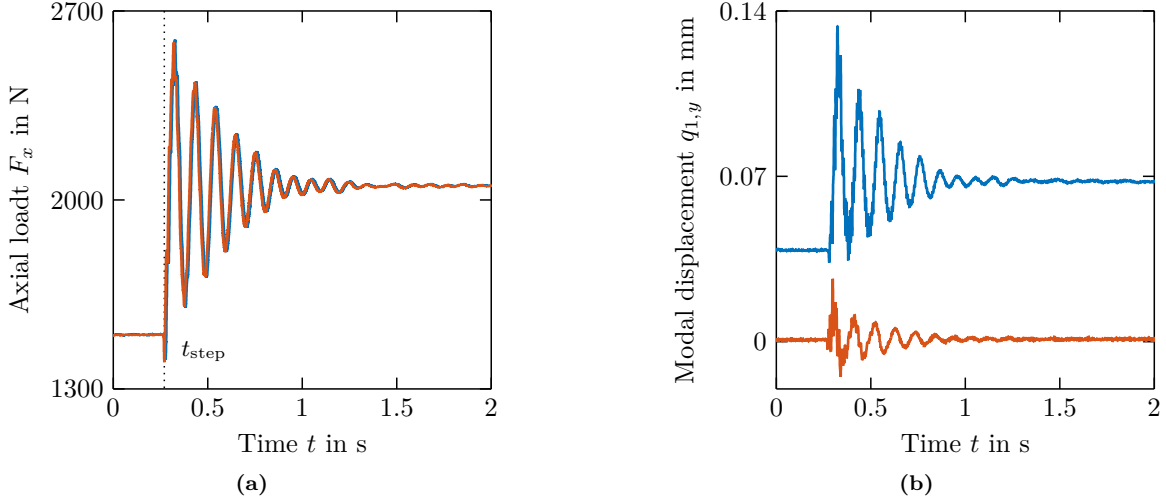


Fig. 9 Beam-column with step-shaped axial load in passive (—) and active (—) configuration, (a) experimental axial load F_x versus time t , (b) modal displacement $q_{1,y}$ of the first mode in y -direction versus time t

In the passive configuration, the initial load already deforms the real, imperfect beam-column. The applied step-shaped axial load amplifies the deformation and there is a high peak displacement. After application of the step-shaped axial load, the modal displacement $q_{1,y}$ has almost doubled.

In the active configuration, the beam-column is again forced into a straight position right away. The step-shaped axial load deforms the beam-column, but the peak displacement as well as the time of oscillation is smaller than in the passive configuration. After application of the step-shaped axial load, the modal displacement $q_{1,y}$ is again reduced to zero.

6 CONCLUSION

In this paper, the gain-scheduled \mathcal{H}_∞ buckling control of an axially loaded beam-column with circular cross-section embedded in piezo-elastic supports is investigated experimentally. The beam-column is subject to time-varying axial loads that influence the lateral dynamic behavior and, eventually, cause the beam-column to buckle. With the piezo-elastic supports, the beam-column is stabilized in arbitrary lateral directions. For the model-based gain-scheduled \mathcal{H}_∞ control, a reduced modal model of the beam-column based on a finite element (FE) model to incorporate the axial load-dependency of the beam-column and to include the dynamics of the electrical components is used. The beam-column plant is a polytopic Linear Parameter-Varying (LPV) system with a defined operating range of the axial load. Thus, the gain-scheduled \mathcal{H}_∞ buckling control guarantees stability and performance for arbitrary trajectories of the axial load within this range. The performance of the controller is designed to include integral action to reduce static beam-column deformations and lateral beam-column vibrations. The implementation of the controller in an experimental test setup shows the effectiveness of the active buckling control for both ramp-shaped and step-shaped axial loads. In the passive configuration without active buckling control, the axially loaded beam-column with circular cross-section exhibits high lateral deformations for axial loads considerably below the critical buckling load. In the active configuration with active buckling control, stabilization and vibration reduction of the beam-column in arbitrary direction is possible. For ramp-shaped axial loads, the gain-scheduled \mathcal{H}_∞ buckling control stabilizes the beam-column for axial loads 19% higher than the passive beam-column. For step-shaped axial loads, the peak deformation of the beam-column is reduced significantly. In future investigations, the limitations of the active approach for time-varying axial loads, a comparison with numerical simulations of the active buckling control and the quantification of uncertainty will be investigated.

ACKNOWLEDGMENTS

The authors like to thank the German Research Foundation (DFG) for funding this project within the Collaborative Research Center (SFB) 805.

References

- [1] Timoshenko, S. P. and Gere, J. M. *Theory of elastic stability*. New York: McGraw-Hill, 1961.
- [2] Lindberg, H. E. and Florence, A. L. *Dynamic Pulse Buckling. Theory and Experiment*. Dordrecht: Springer, 1987.
- [3] Virgin, L. N. *Vibration of axially loaded structures*. New York: Cambridge University Press, 2007.
- [4] Meressi, T. and Paden, B. “Buckling Control of a Flexible Beam Using Piezoelectric Actuators”. In: *Journal of Guidance, Control, and Dynamics* 16 (5 1993), pp. 977–980.
- [5] Wang, Q. S. “Active buckling control of beams using piezoelectric actuators and strain gauge sensors”. In: *Smart Materials and Structures* 19 (6 2010), pp. 1–8.
- [6] Thompson, S. P. and Loughlan, J. “The active buckling control of some composite column strips using piezoceramic actuators”. In: *Composite Structures* 32 (1995), pp. 59–67.
- [7] Berlin, A. A. et al. “MEMS-Based Control of Structural Dynamic Instability”. In: *Journal of Intelligent Material Systems and Structures* 9 (7 1998), pp. 574–586.
- [8] Zenz, G. and Humer, A. “Stability enhancement of beam-type structures by piezoelectric transducers. Theoretical, numerical and experimental investigations”. In: *Acta Mechanica* 226 (12 2015), pp. 3961–3976.
- [9] Enss, G. C., Platz, R., and Hanselka, H. “Uncertainty in loading and control of an active column critical to buckling”. In: *Shock and Vibration* 19 (5 2012), pp. 929–937.
- [10] Enss, G. C. and Platz, R. “Evaluation of uncertainty in experimental active buckling control of a slender beam-column with disturbance forces using Weibull analysis”. In: *Mechanical Systems and Signal Processing* 79 (2016), pp. 123–131.
- [11] Enss, G. C. “Beherrschung von Unsicherheit am Beispiel eines aktiv gegen Knicken stabilisierten Systems”. PhD thesis. Technische Universität Darmstadt, 2016.
- [12] Schaeffner, M., Götz, B., and Platz, R. “Active buckling control of a beam-column with circular cross-section using piezo-elastic supports and integral LQR control”. In: *Smart Materials and Structures* 25 (6 2016), pp. 1–10.
- [13] Schaeffner, M. and Platz, R. “Active buckling control of an imperfect beam-column with circular cross-section using piezo-elastic supports and integral LQR control”. In: *Journal of Physics: Conference Series* 744 (1 2016), pp. 1–12.
- [14] Schaeffner, M. and Platz, R. “Linear Parameter-Varying (LPV) Buckling Control of an Imperfect Beam-Column Subject to Time-Varying Axial Loads”. In: *Model Validation and Uncertainty Quantification, Volume 3. Proceedings of the 35th IMAC, A Conference and Exposition on Structural Dynamics 2017*. (Los Angeles, Anaheim). Ed. by Barthorpe Robert J. et al. Conference proceedings of the Society for Experimental Mechanics series. Cham: Springer International Publishing, 2017, pp. 103–112.
- [15] Hesse, D., Hoppe, F., and Groche, P. “Controlling Product Stiffness by an Incremental Sheet Metal Forming Process”. In: *Procedia Manufacturing* 10 (2017), pp. 276–285.
- [16] Preumont, A. *Vibration Control of Active Structures. An Introduction*. Dordrecht: Kluwer Academic Publishers, 2004.
- [17] Gawronski, W. *Balanced Control of Flexible Structures*. London: Springer-Verlag, 1996.
- [18] Fuller, C. R., Elliott, S. J., and Nelson, P. A. *Active Control of Vibration*. London: Academic Press, 1997.
- [19] Skogestad, S. and Postlethwaite, I. *Multivariable feedback control*. Chichester: John Wiley & Sons, 2001.
- [20] Gu, D.-W., Petkov, P. H., and Konstantinov, M. M. *Robust control design with MATLAB®*. London: Springer, 2013.
- [21] Przemieniecki, J. S. *Theory of Matrix Structural Analysis*. New York: McGraw-Hill, 1968.
- [22] Apkarian, P., Gahinet, P., and Becker, G. “Self-scheduled H_∞ control of linear parameter-varying systems. A design example”. In: *Automatica* 31 (9 1995), pp. 1251–1261.
- [23] Becker, G. and Packard, A. “Robust performance of linear parametrically varying systems using parametrically-dependent linear feedback”. In: *Systems & Control Letters* 23 (3 1994), pp. 205–215.
- [24] Packard, A. “Gain scheduling via linear fractional transformations”. In: *Systems & Control Letters* 22 (2 1994), pp. 79–92.
- [25] Zhou, K. and Doyle, J. C. *Essentials of robust control*. Upper Saddle River: Prentice Hall, 1998.